

UC Berkeley

UC Berkeley Previously Published Works

Title

Additive-Free, Low-Temperature Crystallization of Stable α -FAPbI₃ Perovskite

Permalink

<https://escholarship.org/uc/item/50q3c70b>

Journal

Advanced Materials, 34(9)

ISSN

0935-9648

Authors

Du, Tian
Macdonald, Thomas J
Yang, Ruo Xi
et al.

Publication Date

2022-03-01

DOI

10.1002/adma.202107850

Peer reviewed

Additive-Free, Low-Temperature Crystallization of Stable α -FAPbI₃ Perovskite


Tian Du,* Thomas J. Macdonald, Ruo Xi Yang, Meng Li, Zhongyao Jiang, Lokeshwari Mohan, Weidong Xu, Zhenhuang Su, Xingyu Gao, Richard Whiteley, Chieh-Ting Lin, Ganghong Min, Saif A. Haque, James R. Durrant, Kristin A. Persson, Martyn A. McLachlan, and Joe Briscoe*

Formamidinium lead triiodide (FAPbI₃) is attractive for photovoltaic devices due to its optimal bandgap at around 1.45 eV and improved thermal stability compared with methylammonium-based perovskites. Crystallization of phase-pure α -FAPbI₃ conventionally requires high-temperature thermal annealing at 150 °C whilst the obtained α -FAPbI₃ is metastable at room temperature. Here, aerosol-assisted crystallization (AAC) is reported, which converts yellow δ -FAPbI₃ into black α -FAPbI₃ at only 100 °C using precursor solutions containing only lead iodide and formamidinium iodide with no chemical additives. The obtained α -FAPbI₃ exhibits remarkably enhanced stability compared to the 150 °C annealed counterparts, in combination with improvements in film crystallinity and photoluminescence yield. Using X-ray diffraction, X-ray scattering, and density functional theory simulation, it is identified that relaxation of residual tensile strains, achieved through the lower annealing temperature and post-crystallization crystal growth during AAC, is the key factor that facilitates the formation of phase-stable α -FAPbI₃. This overcomes the strain-induced lattice expansion that is known to cause the metastability of α -FAPbI₃. Accordingly, pure FAPbI₃ p–i–n solar cells are reported, facilitated by the low-temperature (≤ 100 °C) AAC processing, which demonstrates increases of both power conversion efficiency and operational stability compared to devices fabricated using 150 °C annealed films.

1. Introduction

Formamidinium lead triiodide (FAPbI₃) has emerged as a promising candidate for efficient and stable perovskite solar cells (PSC) among the family of metal halide perovskites, particularly compared to the early prototype of methylammonium lead triiodide (MAPbI₃). This is because FAPbI₃ has narrower band gap energy of ≈ 1.45 eV—closer to the Shockley–Queisser optimum^[1]—and is thermally more stable than MAPbI₃.^[2] However, formation of α -phase FAPbI₃ normally requires high temperature annealing (≥ 150 °C) for tens of minutes,^[3] whilst the obtained α -FAPbI₃ is metastable at room temperature as it rapidly degrades into a photoinactive, non-perovskite polymorph (δ -FAPbI₃).^[4] The metastability of the perovskite phase is attributed to the relatively large size of formamidinium (FA⁺), leading to a Goldschmidt tolerance factor > 1 that drives the formation of a hexagonal crystal structure instead of cubic crystal structure.^[5]

T. Du,^[†] T. J. Macdonald, L. Mohan, R. Whiteley, J. Briscoe
School of Engineering and Materials Science and Materials Research
Institute
Queen Mary University of London
London E1 4NS, UK
E-mail: tian.du@fau.de; j.briscoe@qmul.ac.uk
T. Du, Z. Jiang, L. Mohan, C.-T. Lin, M. A. McLachlan
Department of Materials and Centre for Processable Electronics
Imperial College
London W12 0BZ, UK

 The ORCID identification number(s) for the author(s) of this article can be found under <https://doi.org/10.1002/adma.202107850>.

© 2022 The Authors. Advanced Materials published by Wiley-VCH GmbH. This is an open access article under the terms of the Creative Commons Attribution-NonCommercial License, which permits use, distribution and reproduction in any medium, provided the original work is properly cited and is not used for commercial purposes.

^[†]Present address: Institute of Materials for Electronics and Energy Technology (i-MEET), Friedrich-Alexander University Erlangen-Nürnberg, Erlangen, Germany

DOI: 10.1002/adma.202107850

T. J. Macdonald, W. Xu, G. Min, S. A. Haque, J. R. Durrant
Department of Chemistry and Centre for Processable Electronics
Imperial College
London W12 0BZ, UK

R. X. Yang
Materials Science Division
Lawrence Berkeley National Lab
1 Cyclotron Rd. Berkeley, California 94720, USA

M. Li
Key Lab for Special Functional Materials of Ministry of Education
National & Local Joint Engineering Research Center for High-efficiency
Display and Lighting Technology
School of Materials Science and Engineering
and Collaborative Innovation Center of Nano Functional Materials and
Applications
Henan University
Kaifeng 475004, China

To overcome this problem, a widely used strategy is compositional engineering of FAPbI₃ by alloying a small fraction of non-native cations, such as methylammonium (MA⁺), Cs⁺,^[6] Rb⁺,^[7] or non-native anions, such as Br,^[1] Cl,^[8] and pseudohalides.^[9] This forms the so called “mixed perovskites” that are used in most of the state-of-the-art PSCs.^[10] However, compositional tuning is usually at the expense of an unwanted increase of band gap, and the mixed perovskites may suffer from local phase segregation of both the non-native cations^[11] and the halides.^[12] It is thus important to further explore approaches that do not alter the composition of FAPbI₃ for future PSC development. Thus an alternative strategy is to incorporate dopant species into the perovskite precursor solution, including small molecules,^[13] quantum dots,^[14] or 2D perovskites,^[15,16] improving the phase stability of α -FAPbI₃ whilst avoiding band gap change or phase segregation. These works point out the potential effectiveness of modulating the FAPbI₃ crystal surface energy in driving δ -to- α phase transition at lower temperature. The improved α -FAPbI₃ stability may be assigned to the dopant species offsetting the residual strains in the FAPbI₃ lattice, which is reported to be a key factor in stabilizing α -FAPbI₃.^[17,18] However, the additive species potentially induce additional chemical changes in the FAPbI₃ film in the long term, and their quantities are usually small and thus difficult to control in large-scale fabrication. To this end, strategies not reliant on processing additives in the precursor solution are preferred, but are rarely reported.^[19]

Here, we report an additive-free, aerosol-assisted crystallization (AAC) method, reliant on the interaction of vaporized Lewis base solvents with the FAPbI₃ films. We simultaneously achieve crystallization of high-quality α -FAPbI₃ films within 2.5 min at 100 °C and remarkably improved phase stability of the α -FAPbI₃. Further, we demonstrate their suitability for efficient, stable solar cells.

2. Results and Discussion

FAPbI₃ films were deposited by spin-coating a precursor solution containing only lead iodide (PbI₂) and formamidinium iodide (FAI) of equal molar ratio, followed by washing of

antisolvent. To obtain α -FAPbI₃, the two routes investigated in our study are illustrated in **Figure 1a**. As the reference route, α -FAPbI₃ films were crystallized through thermal annealing (TA) at 150 °C for 20 min. For the AAC route, the as-cast films were heated at 100 °C followed by exposure to solvent aerosol, that is, a laminar nitrogen flow containing micrometer-size droplets of the mixture of *N,N*-dimethylformamide (DMF) and dimethyl sulfoxide (DMSO) (9:1 in volume ratio). As the aerosol passes horizontally over the films, some of the droplets vaporize near the film surface and the vapor ingresses into the FAPbI₃ films. As **Figure 1a** and **Figure S1**, Supporting Information, show, the films remain yellowish when dried at 100 °C, comprising mostly δ -FAPbI₃,^[19] and were found to turn black within a few seconds of exposure to the aerosol flow, indicating transformation from δ -FAPbI₃ to α -FAPbI₃.

The aim of using a solvent aerosol is to create a steady laminar flow above the film. This leads to controlled vaporization of the solvent droplets in the aerosol near the film surface, generating a continuous “source” of solvent vapor that homogeneously ingresses into the film. As we have demonstrated previously for aerosol post-crystallization treatment of MAPbI₃ films,^[20] the use of aerosol greatly improves the uniformity and reproducibility of the process compared to a conventional solvent annealing setup. As such, we can achieve uniform crystallization of α -FAPbI₃ on a large 25 × 38 mm² substrate, **Figure S2**, Supporting Information, and can easily be scaled up further as shown in our previous work.^[20]

The X-ray diffraction (XRD) patterns, **Figure 1b**, confirm that the FAPbI₃ film remains in the δ -phase when annealed at 100 °C and forms α -phase upon annealing at 150 °C. In the AAC route, phase-pure α -FAPbI₃ can be obtained within 1 min of the aerosol treatment at 100 °C, with the δ -phase completely removed from the film. Closer inspection of the (001) diffraction peak in **Figure 1c** shows a consistent reduction of peak full width at half maximum (FWHM) with increased treatment time, from 0.189° (TA) to 0.172° (1 min), 0.131° (2.5 min), and 0.121° (5 min), indicating improved crystallinity of the FAPbI₃ films. As a comparison, we also plot in **Figure 1b,c** the XRD pattern of a Cs_{0.02}FA_{0.98}PbI₃ film, a typical “Cs–FA mixed-cation perovskite,” prepared through the standard 150 °C TA route.^[21] A noticeable shift of $2\theta = 0.1^\circ$ toward higher angles is seen showing that Cs has been incorporated into the lattice, accompanied by a narrowing of the (001) peak (FWHM = 0.101°) suggesting superior film crystallinity. The results suggest that, with the same TA processing, FAPbI₃ demonstrate much poorer crystallinity if no Cs is incorporated. However, with the AAC route, we are able to improve crystallinity of phase-pure α -FAPbI₃ closer to that of Cs_{0.02}FA_{0.98}PbI₃, but without any additives or addition of non-native cations or anions.

Surface scanning electron microscopy (SEM) images, **Figure 1d**, show that the TA α -FAPbI₃ film comprises irregularly shaped grains whilst the AAC films show much larger grains in the lateral dimension; the average lateral grain size increases from 310 nm (TA) to 890 nm (AAC 1 min), 1060 nm (2.5 min), and 1170 nm (5 min), **Figure S3**, Supporting Information. This suggests that AAC processing also facilitates growth of the FAPbI₃ grains, as can also be seen from the cross-sectional SEM images. It is worth noting that the “grain” size is not the crystallite size of FAPbI₃, as multiple crystallites can be seen within a

Z. Su, X. Gao
Shanghai Synchrotron Radiation Facility (SSRF)
Zhangjiang Laboratory
Shanghai Advanced Research Institute
Shanghai Institute of Applied Physics
Chinese Academy of Sciences
239 Zhangheng Road, Shanghai 201204, China

J. R. Durrant
SPECIFIC IKC, College of Engineering
Swansea University
Swansea SA2 7AX, UK

K. A. Persson
Molecular Foundry
Lawrence Berkeley National Lab
1 Cyclotron Rd. Berkeley, California 94720, USA

K. A. Persson
Department of Materials Science and Engineering
University of California, Berkeley
210 Hearst Mining Memorial Building, Berkeley, CA 94720, USA

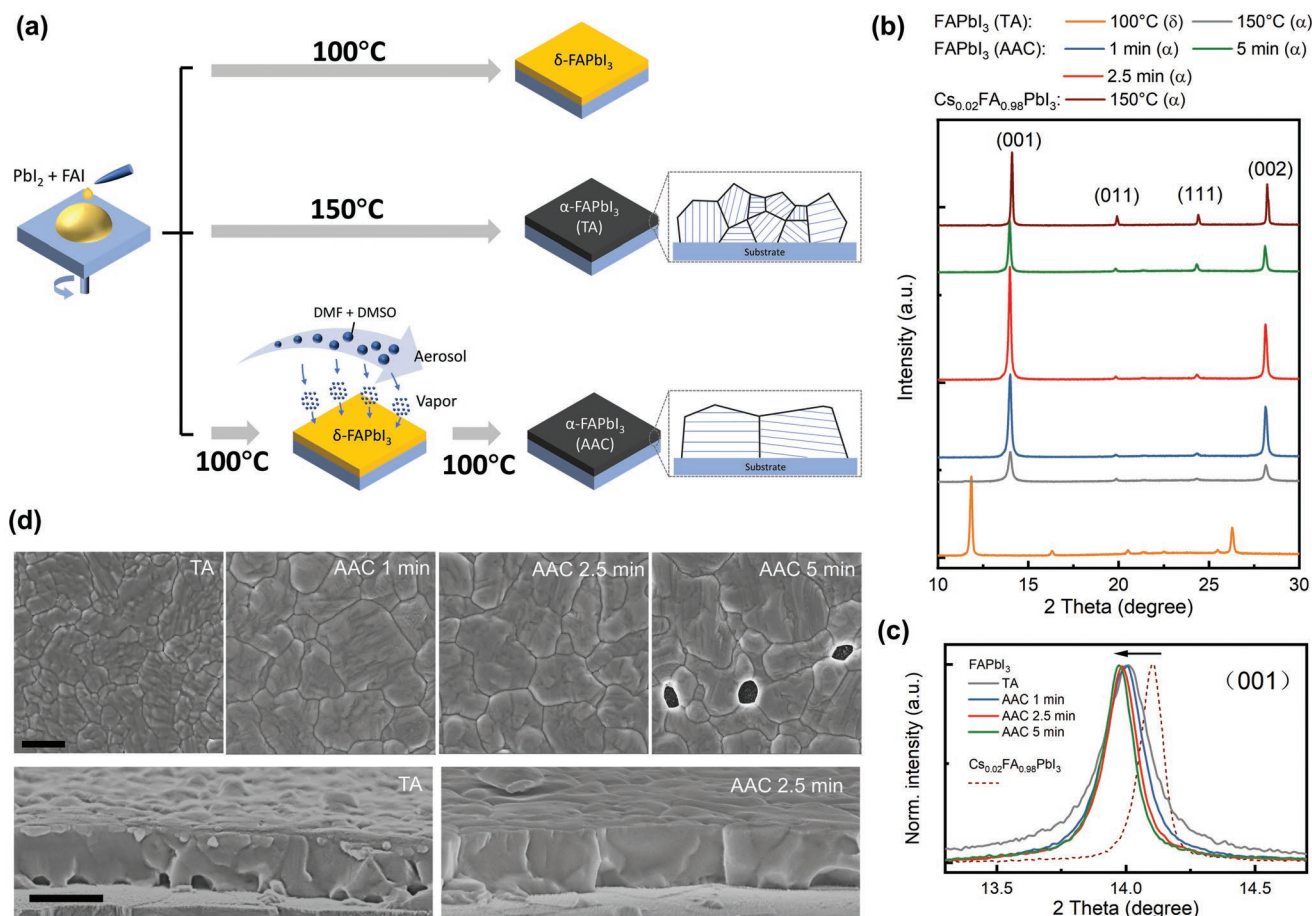


Figure 1. Crystallization FAPbI₃ films. a) Schematic drawing of formation of α -FAPbI₃ through thermal annealing (TA) and aerosol-assisted crystallization (AAC). b) X-ray diffraction patterns (XRD) of FAPbI₃ films and a Cs_{0.02}FA_{0.98}PbI₃ film. c) Zoom-in figure of the (001) peak. d) Top: Surface scanning electron microscopy (SEM) images of FAPbI₃ films via TA and AAC processing of 1, 2.5, and 5 min. Pinholes can be seen on AAC 5 min film. The scale bar is 1 μ m for all images. Bottom: Cross-sectional SEM images of FAPbI₃ films via TA and AAC of 2.5 min. Scale bar is 500 nm for both images.

single “grain,” particularly in the TA film, as such the “grain” is more likely a multi-crystalline cluster,^[22] as is analyzed further below. There is also a time window for effective AAC of FAPbI₃, as aerosol treatment for 5 min has caused noticeable pinhole formation, undesirable for thin-film optoelectronic devices. This is ascribed to the tendency of perovskite grain growth toward a minimization of surface energy, which eventually causes dewetting of the grains from the substrate. Due to the clear pinholes rendering them unsuitable for optoelectronic devices, the 5 min AAC films are not considered further.

The above results suggest solvent vapor reduces the energy barrier of δ -to- α phase transition, thereby enabling lower phase transition temperature. We speculate that this is because DMF/DMSO molecules—owing to their Lewis base nature^[23]—have strong coordination with Pb²⁺ that facilitates the rotation of the [PbI₆]⁴⁻ octahedra. Such coordination drives a configurational transition of the octahedra from face-sharing into corner-sharing and thereby promoting the formation of α -FAPbI₃.^[3,24] This hypothesis is supported by our initial screening of suitable solvents, which indicated that only Lewis base solvents were capable of converting yellow δ -FAPbI₃ to black α -FAPbI₃ (see Table S1, Supporting Information). Owing to the higher boiling

point of DMSO (189 °C), it has to be mixed with DMF that has lower boiling point (153 °C) at maximum 10%_{vol} to avoid condensation of the aerosol at 100 °C (Figure S4, Supporting Information). XRD measurements show that DMF aerosol alone or a DMF/*N*-methyl-2-pyrrolidone (NMP) mixture cannot drive a complete δ -to- α transition at 100 °C (Figure S5, Supporting Information). The exact origin of these differences is likely related to the strength of Lewis basicity of these solvents and is the subject of ongoing studies. Nevertheless, the synergistic effects of lower processing temperature and crystal growth are key factors for strain relaxation and thereby improved stability of α -FAPbI₃, which will be discussed below.

The phase stability of FAPbI₃ was examined by aging the films under 1 Sun illumination in ambient air of 75 \pm 5% relative humidity (RH), in which the high humidity is used to accelerate phase degradation.^[5] As the photographs in Figure 2a show, the TA film rapidly turned yellow within 8 h, consistent with literature report of its metastable nature.^[5] In strong contrast, a remarkable improvement of stability is observed for the AAC films, where nearly no degradation is seen up to 150 h. It is also seen that increased aerosol treatment time from 1 to 2.5 min further improves the film stability. The XRD patterns,

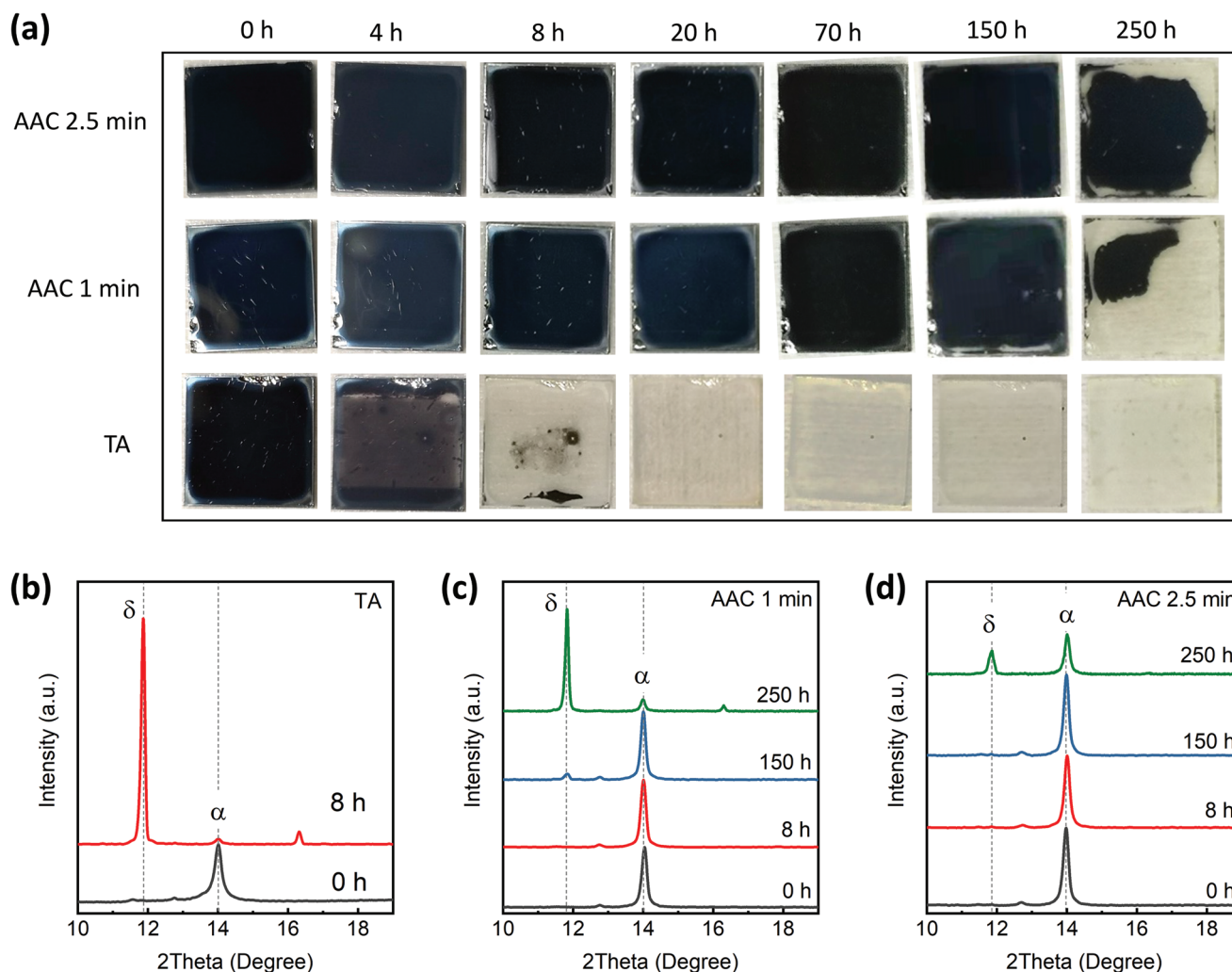


Figure 2. Stability of FAPbI₃ films. a) Photographs of FAPbI₃ films aging under 1 Sun illumination in humid air (75 ± 5% RH) for different times. b–d) XRD patterns obtained at different time of aging of TA FAPbI₃ (0 and 8 h) (b), AAC FAPbI₃ treated for 1 min (0, 8, 150, and 250 h) (c), and 2.5 min (0, 8, 150, and 250 h) (d). The peaks assigned to δ -phase and α -phase are labeled on the plots.

Figure 2b–d, confirm that the main degradation product is δ -FAPbI₃ in all cases. As such the instability is driven by phase degradation instead of chemical degradation, such as formation of PbI₂.^[25]

To elucidate the crystallographic origins of improved phase stability, we first estimate the change of crystallite size (D) and residual lattice strain (ϵ) in the FAPbI₃ films from the XRD peak broadening as defined by the Williamson–Hall (WH) method (see detailed description in Supporting Information)^[26] for the TA film, 1 min AAC film, 2.5 min AAC film and ground FAPbI₃ powders, with the WH plots shown in Figure 3a. The crystallite size can be estimated from the y -axis intercept of the fitting lines, and is plotted in Figure 3b, showing an increase from 51 nm to 88 nm and 154 nm for TA, 1 min AAC and 2.5 min AAC films, respectively, and is 82 nm for the ground powder.

In parallel, lattice strain can be determined from the slope of the fitting line, plotted in Figure 3c, showing a change from –0.04% to 0.02%, 0.05%, and 0.04% for TA, 1 min, 2.5 min AAC films and ground powder, respectively (negative strain

suggests contraction), which indicates a transition from contraction to expansion of the lattice in the out-of-plane direction, that is, perpendicular to the substrate. As substrate adhesion is a main cause of residual strains in thin films, the observed out-of-plane compressive strain in TA films is more likely induced by a more substantial in-plane lattice expansion, with their relative magnitude defined by the Poisson ratio of the materials.^[17] Similarly, the small out-of-plane tensile strain for the AAC films indicates a relaxation of in-plane tensile strain compared to the TA film. Interestingly, the ground powder, which is free from substrate adhesion, exhibits a similar strain to the AAC films. Importantly, this indicates that the AAC processing minimizes the impact of substrate adhesion on the crystal structure of FAPbI₃ films.

We then probe the origin of these lattice distortions by calculating the lattice parameters from the (001), (011), and (111) diffraction peaks, and find a strong deformation from the cubic structure of the lattice in the TA film with remarkable elongation of the a -axis but shortening of both b - and c -axes, whilst both 1 and 2.5 min AAC films show less deformation from a

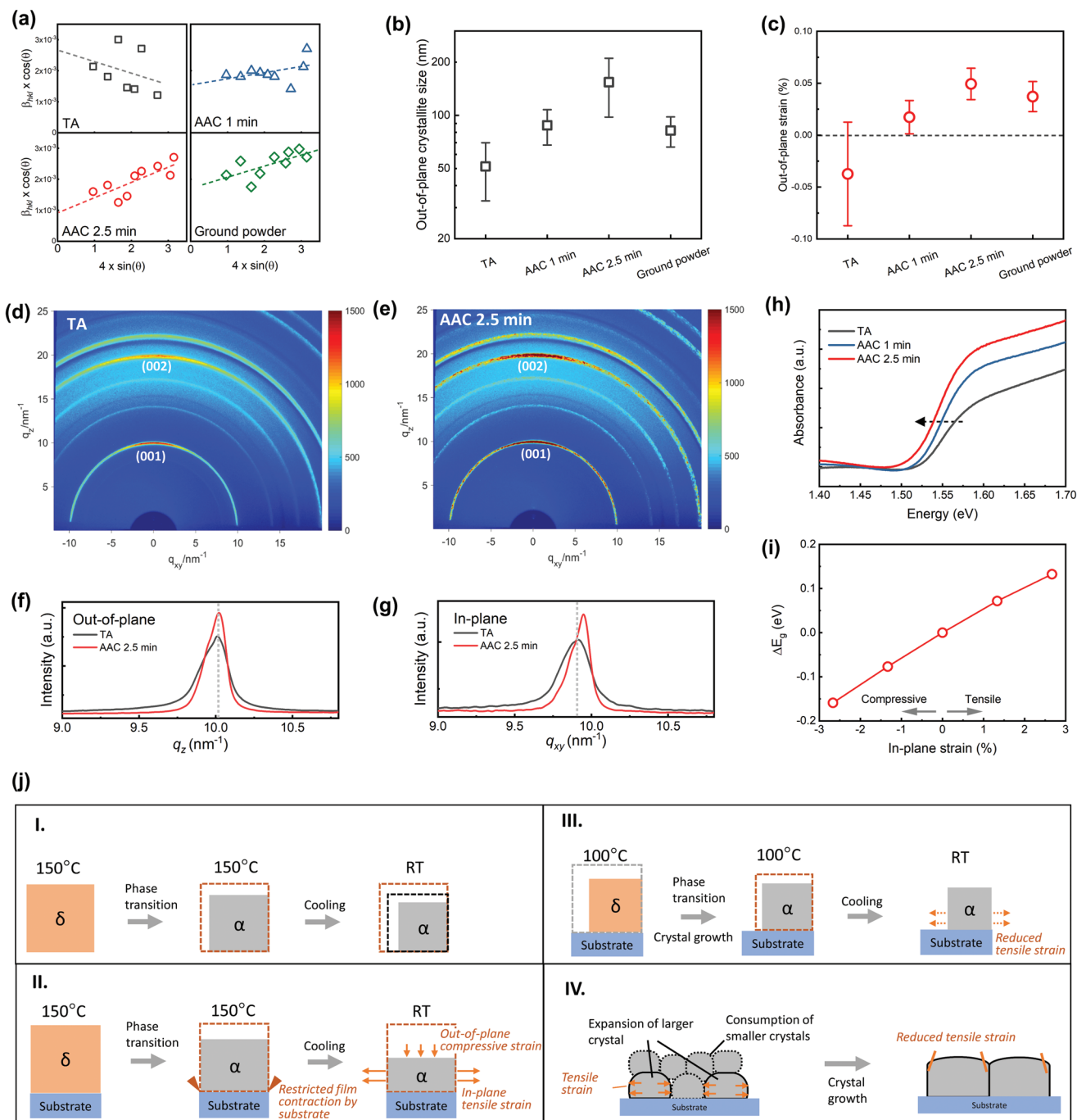


Figure 3. Analysis of crystallite size and strain. a) WH plots of the FAPbI₃ films and ground powders. b) Crystallite size of FAPbI₃ in the out-of-plane direction determined from WH plots. c) Lattice strains in the out-of-plane direction of FAPbI₃ derived from WH plots. Negative (positive) values correspond to out-of-plane compressive (tensile) strain. d,e) 2D GIWAX plots of FAPbI₃ films via the TA route (d) and the 2.5 min AAC route (e). The scale bar is the intensity of diffraction (arb. units). f,g) 1D GIWAX patterns of the TA and 2.5 min AAC FAPbI₃ films in the out-of-plane (f) and in-plane (g) directions. h) UV-vis absorption spectra of the FAPbI₃ films. The arrow indicates the redshift of the absorbance onset. i) First-principle calculation of FAPbI₃ bandgap energy as a function of in-plane strain. Direction of tensile or compressive strain is indicated on the plot. Negative (positive) change of ΔE_g means reduction (increase) of band gap energy. j) Schematic drawing of volume contraction during thermal processing of α -FAPbI₃ owing to phase transition and cooling to room temperature (RT) (I), formation of in-plane tensile strains due to substrate adhesion (II), and relaxation of residual tensile strains in the AAC route through lower processing temperature (III), and the secondary crystal growth during AAC process (IV): the consumption of smaller grains, expansion of larger grains, and reconstruction of grain boundaries that relaxes residual in-plane tensile strains.

cubic structure (Figure S6, Supporting Information). In accordance, TA FAPbI₃ also shows greater unit cell volume (254.50 Å³) than 1 min AAC (254.11 Å³) and 2.5 min AAC (253.85 Å³) films, suggesting lattice expansion that supports the existence of tensile strains in the TA film.

To characterize directly the in-plane tensile strain in more detail we turn to grazing-incidence wide-angle X-ray scattering (GIWAXS) measurements. Figure 3d,e shows the 2D patterns of TA and 2.5 min AAC films. The 1D patterns, Figure 3f,g, plot the (001) peaks along out-of-plane (q_z) and in-plane (q_{xy}) directions, respectively. The out-of-plane (001) peak shows a minimal shift between TA and 2.5 min AAC films, whilst there is a noticeable in-plane peak shift toward lower q_{xy} by 0.05 nm⁻¹ for the TA film. It indicates increased spacing of {100} planes parallel to the substrate and thereby in-plane lattice expansion in the TA film. The observation herein is consistent with the XRD analysis, which together suggests substantial in-plane tensile strain in the TA film compared to AAC films. The in-plane tensile strain transversely contracts the lattice in the out-of-plane direction as observed in XRD but leads to overall lattice volume increase.

It is also observed in the 2D patterns that the majority of diffraction intensities of the TA film are located within a small angle range along the out-of-plane direction (Figure 3b). This inferior in-plane crystallinity of the TA FAPbI₃, as also observed in other studies,^[27,28] is thought to be caused by a highly strained lattice, resulting in poor crystallization in the in-plane directions. This is in contrast to a MAPbI₃ thin film prepared through a similar TA route,^[29] Figure S7, Supporting Information, where the diffraction intensities are uniformly distributed along the (110) ring. The 2D patterns of the 2.5 min AAC film shows that the diffraction intensities are not only higher but also extended in all directions with respect to the substrate (Figure 3e), ascribing to relaxation of in-plane tensile strains thereby increasing crystallinity along the in-plane direction.

To further support the crystallographic analysis of lattice strain, we investigate strain-induced band gap energy (E_g) change in the FAPbI₃ films with first-principles calculations, Figure 3h, which are compared against experimental UV-vis absorption spectra plotted in Figure 3i. The calculation data suggests a decrease of E_g by ≈ 50 meV for a reduction of tensile strain by 1%. Our experimental data show a decrease of E_g by 7 meV in the 2.5 min AAC film compared to the TA film, at the same time as the tensile strain reduces by $\approx 0.2\%$ estimated from volume change. Therefore, both the magnitude and direction of strain change (i.e., reduction in tensile strain) are in excellent agreement between the experimental data and simulation data, supporting our conclusion that in-plane tensile strain is indeed reducing in the AAC films.

Accordingly, we explain the origin of residual tensile strains in the FAPbI₃ films with the four schematic drawings (I, II, III, and IV) in Figure 3j. As Figure 3j(I) shows, converting δ -FAPbI₃ to α -FAPbI₃ is accompanied by substantial lattice contraction, mainly due to an inherent volume reduction during the phase transition (discussed further below) supplemented by thermal contraction upon cooling to room temperature. In-plane tensile strain emerges due to substrate adhesion in the in-plane direction, as perovskites have much larger expansion coefficient than the indium tin oxide (ITO) substrate. Hence,

contraction is mainly allowed only in the out-of-plane direction,^[30] described in Figure 3j(II), leaving a sustained in-plane tensile strain and a corresponding out-of-plane compressive strain.^[31] In the AAC route, Figure 3g(III), the lower processing temperature (100 °C) leads to a smaller lattice expansion at the outset, and the residual tensile strains can be further relaxed by the solvent-induced crystal growth. As Figure 3j(IV) shows, the crystal growth is governed by an Ostwald ripening process,^[20] in which the larger grains grow at the expense of smaller grains. This vapor ingression is maximized at grain boundaries, allowing for a thorough microstructural reconstruction on the edge of existing FAPbI₃ grains toward a more thermodynamically equilibrated configuration, which we postulate drives the relaxation of the residual in-plane tensile strains.

To investigate why lattice compression improves the phase stability of α -FAPbI₃, we performed density functional theory (DFT) calculations of the total energy versus unit cell volume for both α -FAPbI₃ and δ -FAPbI₃, Figure 4. In the simulation, in-plane strain is applied ranging from -8% to $+8\%$ (negative sign for compressive strain and positive sign for tensile strain) within the (100) facet of cubic α -FAPbI₃ (Figure 4a) and within the (001) facet of hexagonal δ -FAPbI₃ (Figure 4b), respectively. The total energy and the volumes are shown at each strain configuration, Figure 4c, indicating that the optimized volume per formula is 256.0 Å³ for the α -phase and 284.6 Å³ for the δ -phase, respectively, rendering a decrease of unit cell volume by 10% during the δ -to- α phase transition. The δ -phase has

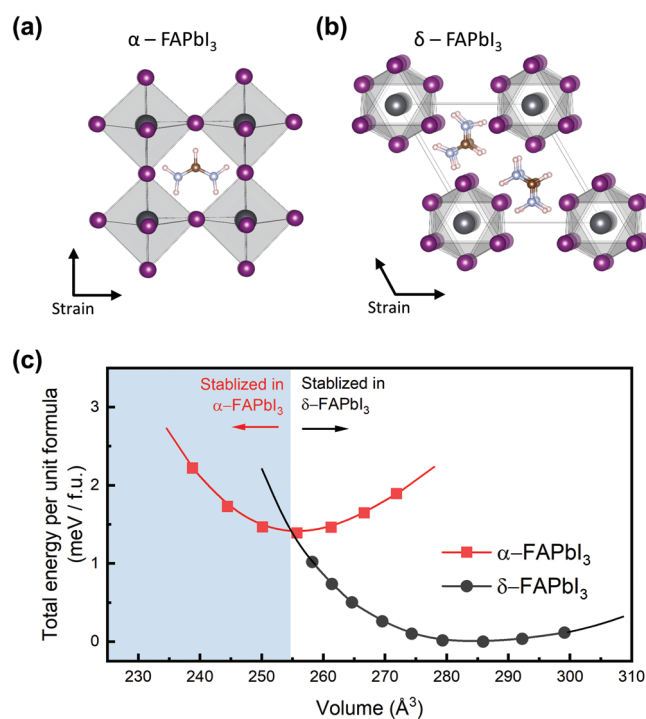


Figure 4. Origin of phase-stability improvement. a,b) Schematic drawing of the crystal structure of cubic α -FAPbI₃ (a) and hexagonal δ -FAPbI₃ (b), the arrows indicate the direction of applied strain in the simulation. Atoms are shown as balls: Pb is dark gray, I is purple, C is brown, N is light blue, H is light brown. c) Density functional theory (DFT) calculation of the total energy per unit formula as a function of unit cell volume for α -FAPbI₃ and δ -FAPbI₃.

a lower total energy than the α -phase at optimized volume, but the total energy of the δ -phase starts to increase upon lattice contraction. The fitted equation-of-states lines show the crossing point of total energy at around 254.7 \AA^3 , below which the α -phase is energetically more favorable than the δ -phase. It can be concluded that the contraction of volume can be considered as an order parameter that drives the δ -to- α -phase transition, indicating compressive strain to be a stabilizing force for α -FAPbI₃. The calculated critical unit cell volume (254.7 \AA^3) is in excellent agreement with the experimental unit cell volume (254.50 \AA^3) of our TA FAPbI₃. This supports the hypothesis that AAC promotes the stability of α -phase FAPbI₃ via lattice contraction, as the experimental unit cell volumes for 1 min AAC (254.11 \AA^3) and 2.5 min AAC (253.85 \AA^3) shift further away from the critical unit cell volume toward the stable region for α -FAPbI₃.

To demonstrate the validity of our DFT calculation and the relevance of the conclusion drawn to broader context, we carried out the same calculation on CsPbI₃ perovskite that is also reported to suffer from degradation from black to yellow phase.^[32] The results are shown in Figure S8, Supporting Information. Contrary to the observations in FAPbI₃, δ -CsPbI₃ has smaller volume than α -CsPbI₃ at their respective lowest total energies, hence increasing the volume of α -CsPbI₃ improves its stability.^[33] The result is in good agreement with the literature that α -CsPbI₃ can be stabilized by introducing tensile strains,^[32]

as opposed to α -FAPbI₃ in which tensile strains should be removed. This opposite behavior is explained by the difference in the Goldschmidt tolerance factor (t) for FAPbI₃ ($t > 1$) and CsPbI₃ ($t < 0.8$).^[5] FA⁺ is too large in size for the cavity of the octahedra hence driving the structure to collapse to a face-sharing non-perovskite phase that bears a larger volume. Thus for FAPbI₃ lattice contraction favors the formation of the higher-density perovskite phase. On the other hand, with Cs⁺ being too small in size, the octahedral network transitioned into a lower-volume edge-sharing phase, and in such case the lower-density perovskite phase is preferentially formed under lattice expansion. Both compositions suffer from the structural instabilities but in opposite ways, which supports the benefit of Cs-FA mix cation perovskites for phase stability.

Finally, we investigate the optoelectronic properties and the performance of these FAPbI₃ films (TA, AAC 1 min and AAC 2.5 min) in solar cells. We measured the photoluminescence (PL) spectra of these films and plot in Figure 5a the peak intensity at different excitation densities, where all films show linear increase of PL with excitation density. The critical observation is an approximate tenfold increase of PL intensity between TA and 1 min AAC films, and an approximate fivefold increase between the 1 min AAC and the 2.5 min AAC film under approximate solar irradiance (100 mW cm^{-2}). The enhancement of PL intensity under solar irradiance, owing to suppression of non-radiative recombination pathways,^[34] is linked to the

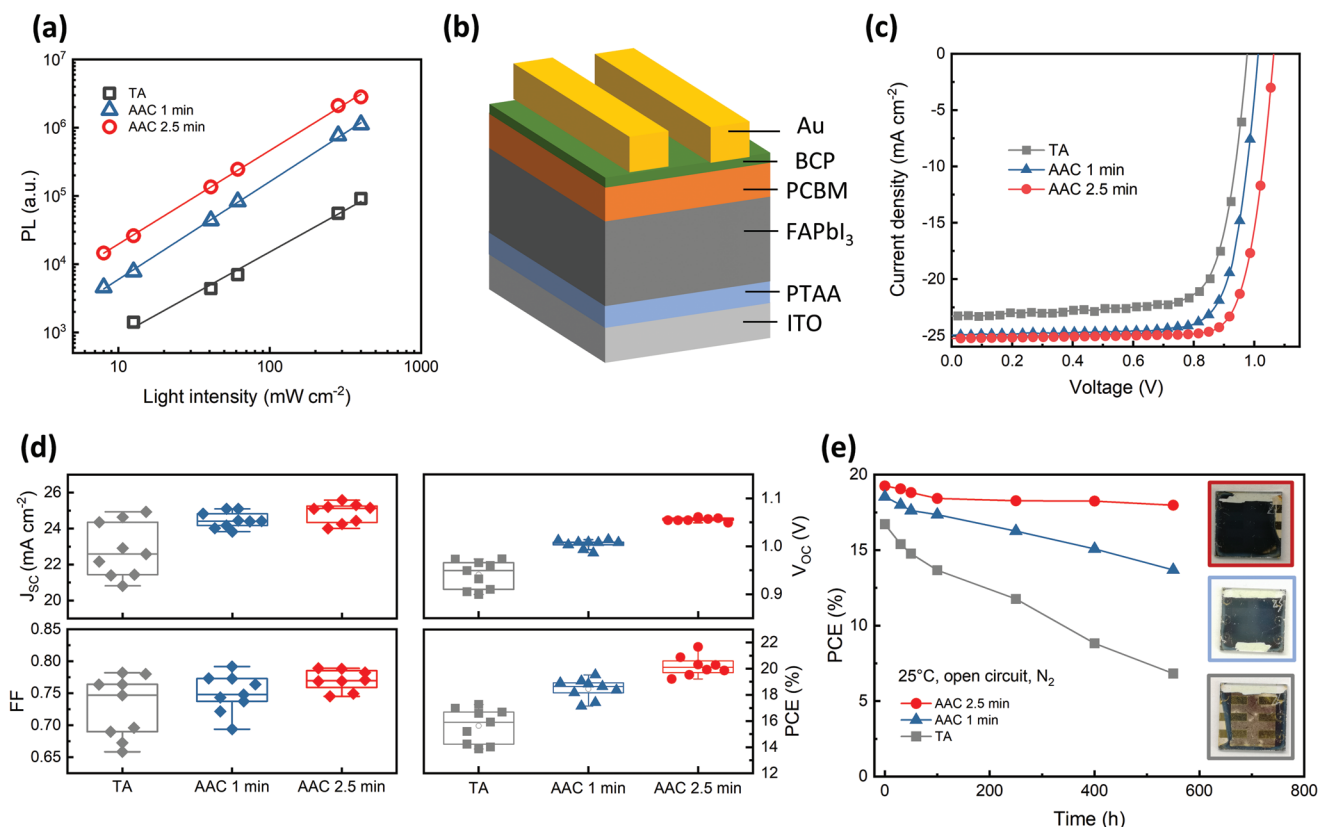


Figure 5. Photoluminescence of FAPbI₃ films and solar cell performance. a) Photoluminescence (PL) yield of the FAPbI₃ films measured with 635 nm monochromatic laser excitation with varied intensity. b) Schematic drawing of the p-i-n structured FAPbI₃ solar cells. c) Representative JV curves of FAPbI₃ solar cells, measured with reverse scan (from open circuit to short circuit) under scan rate of 50 mV s^{-1} . d) Statistical data of photovoltaic parameters. e) Evolution of PCE with time under continuous 1 Sun illumination in nitrogen atmosphere.

change of quasi-Fermi level splitting (ΔE_F) in the FAPbI₃ films according to the generalized Planck's law by approximately $kT \times \ln(10) \approx 60$ mV and by $kT \times \ln(5) \approx 40$ mV, respectively, and indicates the overall improvement in crystalline quality of the perovskite films.^[35]

Facilitated by the reduced processing temperature of FAPbI₃ via AAC, we fabricated solar cells with a p-i-n architecture, Figure 5b, in which poly(triaryl amine) (PTAA) was used as hole-transport layer (HTL) and [6,6]-phenyl-C61butyric acid methyl ester (PCBM) as the electron-transport layer. A bathocuproine (BCP) layer was deposited prior to deposition of Au as the cathode. In this architecture, no annealing process is needed for the contact layers and the full device can be processed ≤ 100 °C giving advantages for flexible devices and two-terminal tandem solar cells.^[36] The current density–voltage (J - V) curves of representative devices, Figure 5c, highlight that AAC route improves both J_{SC} and V_{OC} of the FAPbI₃ solar cells compared to the TA route, whilst longer AAC time further increases V_{OC} . These devices show no noticeable J - V hysteresis when the scanning direction is altered (Figure S9, Supporting Information). The external quantum efficiency (EQE) spectra of the three devices plotted in Figure S10, Supporting Information, show integrated J_{SC} are 23.1, 23.8, and 24.2 mA cm⁻² for TA, 1 min AAC and 2.5 min AAC devices, within a reasonable range of deviation compared to the J_{SC} measured from JV scans. The statistical data of photovoltaic parameters measured from multiple devices, Figure 5d and Table 1, highlight an increase of average (champion) PCE from 15.6% (17.2%) to 18.5% (19.5%) and 20.2% (21.6%) and synergistic improvement of all photovoltaic parameters (J_{SC} , V_{OC} , and FF) that in parallel show narrowed statistical distribution. In particular, the increase of V_{OC} , which is 64 mV (TA vs 1 min AAC) and 51 mV (1 min vs 2.5 min AAC), are in qualified agreement with the respective changes of ΔE_F estimated from PL spectroscopy that are 60 and 40 mV, suggesting that the improvement of solar cell performance is directly correlated to the improved quality of FAPbI₃ active layer. Here the relatively low PCEs (<17%) of control devices are due to the poor crystallinity of TA α -FAPbI₃ since we incorporate no additives during film processing,^[15] in contrast to the majority of the literature, where additives are essential in fabricating FAPbI₃ based solar cells.^[8,9,14,21,27,37] Furthermore, our work is the first report of a pure FAPbI₃, p-i-n PSC, and our champion PCE of 21.6% is close to highest-reported PCE for a MA-free, p-i-n PSC (22.7%),^[38] which incorporates 18% Cs and uses a long chain alkylammonium salt as a passivating agent. Hence the ability of our method to bring up PCEs to >21% without additives highlights the important impact of improved crystallinity and strain relaxation that we have achieved on device performance.

Table 1. Photovoltaic parameters of FAPbI₃ solar cells.

	J_{SC} [mA cm ⁻²]	V_{OC} [mV]	FF	PCE (champion) [%]
TA	22.8 ± 1.5	941 ± 30	0.728 ± 0.049	15.6 ± 1.3 (17.2)
AAC 1 min	24.5 ± 0.4	1005 ± 9	0.750 ± 0.030	18.5 ± 0.8 (19.5)
AAC 2.5 min	24.9 ± 0.6	1056 ± 4	0.770 ± 0.016	20.2 ± 0.8 (21.6)

Finally, we correlate solar cell stability with the film stability by showing in Figure 5e the evolution of PCE under continuous 1 Sun illumination in a nitrogen atmosphere. During the initial 100 h, the TA device exhibits rapid PCE drop with aging time, while the aging speed is reduced in the 1 min AAC device and significantly more so in the 2.5 min AAC device. The inset figures show photographs of the ITO side of FAPbI₃ solar cells after aging for 550 h. We can see the TA device turns yellowish and transparent, while the 1 min AAC device becomes gray and the 2.5 min AAC device remains black. XRD patterns of the degraded devices, Figure S11, Supporting Information, show that α -to- δ transition is the key factor driving device performance degradation in inert atmosphere. This shows that the metastability of α -phase poses a critical challenge for FAPbI₃ solar cells even if they are encapsulated, but can be effectively overcome by employing AAC of FAPbI₃ films.

3. Conclusions

We have demonstrated an additive-free method to crystallize phase-pure α -FAPbI₃ at 100 °C in only 1 min and stabilize the α -FAPbI₃ film by modulating the residual strains. An aerosol of Lewis base solvents reduces the energy barrier for δ -to- α phase transition thereby lowering the phase transition temperature. Relaxation of the residual tensile strains, left by substrate restriction of lattice contraction, is identified as a key factor stabilizing α -FAPbI₃ both experimentally and computationally. The lower processing temperature and post-crystallization crystal growth, both enabled by ingress of solvent aerosol, play critical roles in achieving relaxation of residual tensile strains. The as-prepared α -FAPbI₃ films show remarkable improvement of PL yield, which tracks the change of V_{OC} . The solar cells show simultaneous improvement of PCE and operational stability. Our study demonstrates the feasibility of preparing high-quality, phase-pure, and stable α -FAPbI₃ without additives or doping for solar cell applications. In particular, the ability to fabricate high-quality α -FAPbI₃ films in a short time at low-temperature with large-area uniformity, as well as demonstrating high-efficiency, pure FAPbI₃ p-i-n PSCs, opens up wider possibilities for scalable fabrication of FAPbI₃-based solar cells on flexible substrates.

4. Experimental Section

FAPbI₃ Film Deposition: The precursor solutions for all FAPbI₃ films were prepared by dissolving equimolar concentrations (1.25 mol dm⁻³) of PbI₂ (99.985%, TCI) and FAI (GreatCell Solar) in a mixed solvent of DMF and NMP in a volume ratio of 7:3. The solution was stirred at 50 °C until the precursors were dissolved. Deposition of FAPbI₃ was carried out in a nitrogen-filled glovebox. 40 μ L precursor solution was dropped onto each substrate and spun at 3600 rpm for 20 s. At the 9th second, 0.5 mL diethyl ether was dripped onto the spinning substrate. The films were then dried on a hot plate at 100 °C for 2 min.

The reference FAPbI₃ films were then thermally annealed (TA) at 150 °C for 20 min in a nitrogen-filled glovebox. For AAC processing, the yellow films were placed in a cylindrical reactor that was pre-heated at 100 °C. The solvents for AAC are mixture of DMF and DMSO in volume ratio of 9:1. The aerosol was generated using a piezoelectric ultrasonic generator and was carried into the reactor by nitrogen flow at

0.5 dm³ min⁻¹. After the aerosol generation was turned off, the reactor was kept purging with N₂ flow while the samples were left on the heated graphite block for a further 2 min, after that the samples were cooled to room temperature before being removed.

FAPbI₃ Film Characterization: The aging of FAPbI₃ films was carried out in an environmental chamber (75 ± 5% RH) with an automatic humidity controller. The films were illuminated by a white-light LED set at 1 Sun intensity (100 mW cm⁻²). Photographs were taken and XRD measurements were carried out on the aged FAPbI₃ films at different times during the ageing process.

The SEM images were obtained using a LEO Gemini 1525 field emission gun scanning electron microscope. The working voltage of SEM was set at 3 kV. All films were coated with a thin Cr layer of ≈10 nm prior to imaging. XRD patterns for phase identification were obtained with a Bruker D2 PHASER diffractometer. XRD patterns for WH analysis and lattice parameter calculation were obtained with X'Pert Powder diffractometer (PANalytical), Cu Kα (λ = 1.5406 Å) source. The position (2θ) and the FWHM (2θ) of diffraction peaks were determined using a Gaussian fit of the patterns.

Photoluminescence spectroscopy was measured with a Horiba FL 1039 spectrometer, illuminated with monochromatic laser with excitation wavelength of 550 nm. The intensity of the laser was calibrated by a power meter and was tuned with neutral density filters. Ultraviolet-visible (UV-vis) absorption spectra were measured with an Agilent Cary 60 UV-vis spectrophotometer. In all cases the perovskite films are deposited on glass substrates and were coated with a poly(methyl methacrylate) (PMMA) layer.

GIWAXS was carried out at the BL14B1 beamline of the Shanghai Synchrotron Radiation Facility (SSRF), with X-rays with wavelength of 1.2398 Å and energy of 10 keV. 2D GIWAXS patterns were observed from a MarCCD 225 detector. The distance from sample to detector was 320 mm. After that, the 2D GIWAXS patterns were parsed through the FIT2D software. Resultant patterns were demonstrated in scattering vector *q* coordinates according to the formula of $q = 4\pi\sin\theta/\lambda$, where θ corresponds to half of the diffraction angle, and λ is the X-ray wavelength.

Synthesis of FAPbI₃ Powder: FAPbI₃ powder was obtained by grinding as-synthesized single crystals. First, a 0.8 mol dm⁻³ FAPbI₃ solution was prepared in γ -butyrolactone (GBL) and filtered using a poly(tetrafluoroethylene) (PTFE) filter (0.2 μ m pore size). ≈0.4 mL of the filtrate was placed in a 7 mL tall narrow vial and placed into a custom-made metal heating block which was pre-heated to 80 °C. The temperature was gradually increased to 115 °C (≈5 °C h⁻¹) and kept for 3 h. The final crystal size was further increased by heating to a maximum temperature of 119 °C by increasing the temperature by 2 °C h⁻¹. It was noted that slow temperature increments are absolutely necessary to ensure uniform crystal growth. The single crystals were taken out of the vials and ground into fine powders using a pestle.

Density Functional Theory Calculation: The simulation was carried out using the quantum chemistry code Quantum Espresso. The PBEsol functional and the corresponding PAW pseudopotentials with 90 Ry kinetic cut-off energy and 8 × 8 × 8 k-points mesh were used. In-plane strain ranging from -8% to +8% (negative sign for compressive strain and positive sign for tensile strain) was applied for the (100) facet of cubic phase and (001) facet of yellow phase, respectively. The in-plane lattice parameters were varied according to the strain and kept fixed, while the third axis was allowed to relax, resulting in an optimized geometry.

Solar Cell Fabrication and Testing: All devices were fabricated on ITO-coated glass substrates sequentially cleaned in acetone, isopropyl alcohol, and deionized water (using ultrasonics) for 10 min. The substrates were dried using N₂ flow. Prior to deposition the substrates were treated by oxygen plasma for 10 min. PTAA (2 mg mL⁻¹ in chlorobenzene) was spin-coated onto the ITO at 5000 rpm for 15 s as HTL. After drying for 1 min, poly[(9,9-bis(3'-(*N,N*-dimethyl)-*N*-ethylammonium)-propyl)-2,7-fluorene]-*alt*-2,7-(9,9-dioctylfluorene)] (PFN-Br, 0.05 wt% in methanol) was spin-coated onto the HTLs at 5000 rpm for 15 s as interfacial modifier to reduce surface hydrophobicity. Solutions of the electron-transport material were prepared by dissolving 23 mg mL⁻¹ PCBM (99% purity, Ossila) in chlorobenzene. The solution

was stirred at 40 °C for 1 h and filtered through a 0.45 μ m PTFE filter before use. The PCBM solution was spin-coated on to FAPbI₃ films at 1500 rpm for 45 s. An ultrathin interfacial dipole layer was prepared by spin-coating a BCP solution (0.5 mg mL⁻¹ in methanol) on top of PCBM layer at 5000 rpm for 15 s. Finally, the devices were completed by thermally evaporating 100 nm of Au (0.2 Å s⁻¹) at a base pressure of 5 × 10⁻⁶ mbar.

Current density–voltage (*J*–*V*) characteristics were measured using a Keithley 2400 source meter. The cells were illuminated by an AM 1.5 filtered xenon lamp (Oriel Instruments) at 1 sun intensity (100 mW cm⁻²), calibrated using a silicon reference photodiode. The scan rate was fixed at 50 mV s⁻¹ in both forward and reverse directions. EQE spectra were measured with a PV Measurements QEX10 system. The spectral response was calibrated with a silicon reference photodiode. Stability of FAPbI₃ solar cells was characterized by aging the solar cells in inert atmosphere under open circuit condition and measuring the evolution of PCE at different times by *J*–*V* scan. The solar cells were continuously illuminated by white-light LEDs with 1 Sun equivalent intensity.

Supporting Information

Supporting Information is available from the Wiley Online Library or from the author.

Acknowledgements

The authors would like to thank the EPSRC Plastic Electronics CDT (EP/L016702/1) for financial support and provision of equipment resource. J.B. and T.D. acknowledge the QMUL-EPSRC Impact Accelerator Account for financial support. T.D. gratefully acknowledges the Stephen and Anna Hui Scholarship (Imperial College London) for financially supporting his doctoral studies. T.J.M. would like to thank the Royal Commission for the Exhibition of 1851 for their financial support through a Research Fellowship. Computational work was supported by the US Department of Energy, Office of Science, Office of Basic Energy Sciences, Materials Sciences and Engineering Division under contract no. DE-AC02-05-CH11231 (Materials Project program KC23MP). C.-T.L., J.R.D., and M.A.M. acknowledge the Global Research Laboratory (GRL) Program through the National Research Foundation of Korea (NRF) funded by the Ministry of Science and ICT (NRF-2017K1A1A2013153).

Conflict of Interest

The authors declare no conflict of interest.

Author Contributions

T.D. and J.B. conceived the ideas and planned the experiments. T.D. carried out the proof-of-concept experiments, optimized the film deposition conditions and optimized the key AAC processing parameters. T.D. and T.J.M. optimized solar cells fabrication. T.J.M. synthesized the powder samples and is supervised by S.A.H. R.X.Y. performed DFT calculations, which were supervised by K.A.P. M.L., Z.S., and X.G. performed the GIWAXS measurements and analysis. Z.J. assisted with the set-up of the environmental chamber and film aging measurements. L.M. took SEM images and assisted optimizing the AAC set up. W.X. performed PL measurement, supervised by J.R.D. R.W. and G.M. carried out XRD measurements and the WH analysis. C.-T.L. assisted optimizing film deposition and solar cell fabrication. J.B. and M.A.M. supervised the project. T.D. and J.B. planned the manuscript. T.D. wrote the draft of manuscript that was revised by T.J.M., R.X.Y., M.A.M., and J.B. All the authors contributed to the analysis and discussion of the results, as well as, editing of the final manuscript.

Data Availability Statement

Research data are not shared.

Keywords

additive-free, aerosol-assisted crystallization, formamidinium lead triiodide, stability, strain

Received: September 30, 2021

Revised: November 18, 2021

Published online: January 23, 2022

- [1] G. E. Eperon, S. D. Stranks, C. Menelaou, M. B. Johnston, L. M. Herz, H. J. Snaith, *Energy Environ. Sci.* **2014**, *7*, 982.
- [2] E. Smecca, Y. Numata, I. Deretzi, G. Pellegrino, S. Boninelli, T. Miyasaka, A. La Magna, A. Alberti, *Phys. Chem. Chem. Phys.* **2016**, *18*, 13413.
- [3] P. Ahlawat, A. Hinderhofer, E. A. Alharbi, H. Lu, A. Ummadisingu, H. Niu, M. Invernizzi, S. M. Zakeeruddin, M. I. Dar, F. Schreiber, A. Hagfeldt, M. Grätzel, U. Rothlisberger, M. Parrinello, *Sci. Adv.* **2021**, *7*, eabe3326.
- [4] S. Masi, A. F. Gualdrón-Reyes, I. Mora-Seró, *ACS Energy Lett.* **2020**, *5*, 1974.
- [5] Z. Li, M. Yang, J. S. Park, S. H. Wei, J. J. Berry, K. Zhu, *Chem. Mater.* **2016**, *28*, 284.
- [6] M. Saliba, T. Matsui, J.-Y. Seo, K. Domanski, J.-P. Correa-Baena, M. K. Nazeeruddin, S. M. Zakeeruddin, W. Tress, A. Abate, A. Hagfeldt, M. Grätzel, *Energy Environ. Sci.* **2016**, *9*, 1989.
- [7] M. Saliba, T. Matsui, K. Domanski, J.-Y. Seo, A. Ummadisingu, S. M. Zakeeruddin, J.-P. Correa-Baena, W. R. Tress, A. Abate, A. Hagfeldt, M. Grätzel, *Science* **2016**, *354*, 206 LP.
- [8] M. Kim, G. H. Kim, T. K. Lee, I. W. Choi, H. W. Choi, Y. Jo, Y. J. Yoon, J. W. Kim, J. Lee, D. Huh, H. Lee, S. K. Kwak, J. Y. Kim, D. S. Kim, *Joule* **2019**, *3*, 2179.
- [9] J. Jeong, M. Kim, J. Seo, H. Lu, P. Ahlawat, A. Mishra, Y. Yang, M. A. Hope, F. T. Eickemeyer, M. Kim, Y. J. Yoon, I. W. Choi, B. P. Darwich, S. J. Choi, Y. Jo, J. H. Lee, B. Walker, S. M. Zakeeruddin, L. Emsley, U. Rothlisberger, A. Hagfeldt, D. S. Kim, M. Grätzel, J. Y. Kim, *Nature* **2021**, *592*, 381.
- [10] N. J. Jeon, J. H. Noh, W. S. Yang, Y. C. Kim, S. Ryu, J. Seo, S. Il Seok, *Nature* **2015**, *517*, 476.
- [11] K. Domanski, B. Roose, T. Matsui, M. Saliba, S. H. Turren-Cruz, J. P. Correa-Baena, C. R. Carmona, G. Richardson, J. M. Foster, F. De Angelis, J. M. Ball, A. Petrozza, N. Mine, M. K. Nazeeruddin, W. Tress, M. Grätzel, U. Steiner, A. Hagfeldt, A. Abate, *Energy Environ. Sci.* **2017**, *10*, 604.
- [12] E. T. Hoke, D. J. Slotcavage, E. R. Dohner, A. R. Bowring, H. I. Karunadasa, M. D. McGehee, *Chem. Sci.* **2015**, *6*, 613.
- [13] A. Q. Alanazi, D. J. Kubicki, D. Prochowicz, E. A. Alharbi, M. E. F. Bouduban, F. Jahanbakhshi, M. Mladenović, J. V. Milić, F. Giordano, D. Ren, A. Y. Alyamani, H. Albrithen, A. Albadi, M. H. Alotaibi, J. E. Moser, S. M. Zakeeruddin, U. Rothlisberger, L. Emsley, M. Grätzel, *J. Am. Chem. Soc.* **2019**, *141*, 17659.
- [14] S. Masi, C. Echeverría-Arroondo, K. M. M. Salim, T. T. Ngo, P. F. Mendez, E. López-Fraguas, D. F. Macias-Pinilla, J. Planellas, J. I. Climente, I. Mora-Seró, *ACS Energy Lett.* **2020**, *5*, 418.
- [15] J. W. Lee, Z. Dai, T. H. Han, C. Choi, S. Y. Chang, S. J. Lee, N. De Marco, H. Zhao, P. Sun, Y. Huang, Y. Yang, *Nat. Commun.* **2018**, *9*, 3021.
- [16] Y. Liu, S. Akin, A. Hinderhofer, F. T. Eickemeyer, H. Zhu, J. Y. Seo, J. Zhang, F. Schreiber, H. Zhang, S. M. Zakeeruddin, A. Hagfeldt, M. I. Dar, M. Grätzel, *Angew. Chem., Int. Ed.* **2020**, *59*, 15688.
- [17] Y. Chen, Y. Lei, Y. Li, Y. Yu, J. Cai, M. H. Chiu, R. Rao, Y. Gu, C. Wang, W. Choi, H. Hu, C. Wang, Y. Li, J. Song, J. Zhang, B. Qi, M. Lin, Z. Zhang, A. E. Islam, B. Maruyama, S. Dayeh, L. J. Li, K. Yang, Y. H. Lo, S. Xu, *Nature* **2020**, *577*, 209.
- [18] X. Zheng, C. Wu, S. K. Jha, Z. Li, K. Zhu, S. Priya, *ACS Energy Lett.* **2016**, *1*, 1014.
- [19] H. Lu, Y. Liu, P. Ahlawat, A. Mishra, W. R. Tress, F. T. Eickemeyer, Y. Yang, F. Fu, Z. Wang, C. E. Avalos, B. I. Carlsen, A. Agarwalla, X. Zhang, X. Li, Y. Zhan, S. M. Zakeeruddin, L. Emsley, U. Rothlisberger, L. Zheng, A. Hagfeldt, M. Grätzel, *Science* **2020**, *370*, 6512.
- [20] T. Du, S. R. Ratnasingham, F. U. Kosasih, T. J. Macdonald, L. Mohan, A. Augurio, H. Ahli, C.-T. Lin, S. Xu, W. Xu, R. Binions, C. Ducati, J. R. Durrant, J. Briscoe, M. A. McLachlan, *Adv. Energy Mater.* **2021**, *11*, 2101420.
- [21] J. W. Lee, Z. Dai, C. Lee, H. M. Lee, T. H. Han, N. De Marco, O. Lin, C. S. Choi, B. Dunn, J. Koh, D. Di Carlo, J. H. Ko, H. D. Maynard, Y. Yang, *J. Am. Chem. Soc.* **2018**, *140*, 6317.
- [22] W. Li, S. K. Yadavalli, D. Lizarazo-Ferro, M. Chen, Y. Zhou, N. P. Padture, R. Zia, *ACS Energy Lett.* **2018**, *3*, 2669.
- [23] N. Ahn, D. Y. Son, I. H. Jang, S. M. Kang, M. Choi, N. G. Park, *J. Am. Chem. Soc.* **2015**, *137*, 8696.
- [24] X. Cao, L. Zhi, Y. Li, F. Fang, X. Cui, Y. Yao, L. Ci, K. Ding, J. Wei, *ACS Appl. Mater. Interfaces* **2017**, *9*, 32868.
- [25] T. Du, C. H. Burgess, J. Kim, J. Zhang, J. R. Durrant, M. A. McLachlan, *Sustainable Energy Fuels* **2017**, *1*, 119.
- [26] G. K. Williamson, W. H. Hall, *Acta Metall.* **1953**, *1*, 22.
- [27] H. Min, M. Kim, S. U. Lee, H. Kim, G. Kim, K. Choi, J. H. Lee, S. Il Seok, *Science* **2019**, *366*, 749.
- [28] M. C. Tang, Y. Fan, D. Barrit, X. Chang, H. X. Dang, R. Li, K. Wang, D. M. Smilgies, S. F. Liu, S. De Wolf, T. D. Anthopoulos, K. Zhao, A. Amassian, *J. Mater. Chem. A* **2020**, *8*, 1095.
- [29] T. Du, W. Xu, S. Xu, S. R. Ratnasingham, C.-T. Lin, J. Kim, J. Briscoe, M. McLachlan, J. Durrant, *J. Mater. Chem. C* **2020**, *8*, 12648.
- [30] D. Xue, Y. Hou, S. Liu, M. Wei, B. Chen, Z. Huang, Z. Li, B. Sun, A. H. Proppe, Y. Dong, M. I. Saidaminov, S. O. Kelley, J. Hu, E. H. Sargent, *Nat. Commun.* **2020**, *11*, 1514.
- [31] D. Liu, D. Luo, A. N. Iqbal, K. W. P. Orr, T. A. S. Doherty, Z. Lu, S. D. Stranks, W. Zhang, *Nat. Mater.* **2021**, *20*, 1337.
- [32] Y. Wang, M. I. Dar, L. K. Ono, T. Zhang, M. Kan, Y. Li, L. Zhang, X. Wang, Y. Yang, X. Gao, Y. Qi, M. Grätzel, Y. Zhao, *Science* **2019**, *365*, 591.
- [33] J. A. Steele, H. Jin, I. Dovgaliuk, R. F. Berger, T. Braeckvelt, H. Yuan, C. Martin, E. Solano, K. Lejaeghere, S. M. J. Rogge, C. Notebaert, W. Vandezande, K. P. F. Janssen, B. Goderis, E. Debroye, Y. Wang, Y. Dong, D. Ma, M. Saidaminov, H. Tan, Z. Lu, V. Dyadkin, J. Hofkens, M. B. J. Roelofs, *Science* **2019**, *684*, 679.
- [34] T. Du, W. Xu, M. Daboczi, J. Kim, S. Xu, C. T. Lin, H. Kang, K. Lee, M. J. Heeney, J. S. Kim, J. R. Durrant, M. A. McLachlan, *J. Mater. Chem. A* **2019**, *7*, 18971.
- [35] T. Du, J. Kim, J. Ngiam, S. Xu, P. R. F. Barnes, J. R. Durrant, M. A. McLachlan, *Adv. Funct. Mater.* **2018**, *28*, 1801808.
- [36] X. Lin, D. Cui, X. Luo, C. Zhang, Q. Han, Y. Wang, L. Han, *Energy Environ. Sci.* **2020**, *13*, 3823.
- [37] J. Wang, S. Luo, Y. Lin, Y. Chen, Y. Deng, Z. Li, K. Meng, G. Chen, T. Huang, S. Xiao, H. Huang, C. Zhou, L. Ding, J. He, J. Huang, Y. Yuan, *Nat. Commun.* **2020**, *11*, 582.
- [38] S. Gharibzadeh, P. Fassel, I. M. Hossain, P. Rohrbeck, M. Frericks, M. Schmidt, T. Duong, M. R. Khan, T. Abzieher, B. A. Nejad, F. Schackmar, O. Almora, T. Feeney, R. Singh, D. Fuchs, U. Lemmer, J. P. Hofmann, S. A. L. Weber, U. W. Paetzold, *Energy Environ. Sci.* **2021**, *14*, 5875.